Thermoacoustic Instabilities in Gas Turbines and Rocket Engines: Industry meets Academia
May 30 – June 02, 2016
Munich, Germany
Paper No.: GTRE-021

Detection of direct and indirect noise generated by synthetic hot spots in a duct

Francesca De Domenico[1], Erwan Rolland[1], Simone Hochgreb[1]

Abstract

Indirect noise generated by the acceleration of entropy or vorticity perturbations through a nozzle is of interest both as an additional source of transmitted noise, but also as a source of combustion instabilities via backward propagating waves. There is a lack of experimental data, mostly due to difficulties in separating direct and indirect noise. Previous experiments attempted to isolate indirect noise by generating thermoacoustic hot spots electrically and measuring the transmitted acoustic waves, yet there is no data on the reflected or backward propagating acoustic waves. In this work, synthetic hot spots are generated by unsteady electrical heating of thin wires. These hot spots are accelerated through an orifice plate, producing a strong acoustic signature upstream of the orifice plate. Using a time separation argument, we identify the indirect noise signal, showing that its contribution to the overall noise is not negligible in either in subsonic or sonic throat conditions. However, the amplitude of direct noise is larger, making indirect noise difficult to identify if the two contributions are merged. We demonstrate the importance of appropriate pressure transducer instrumentation and accounting for the respective transfer functions in order to account for low frequency effects in the determination of pressure.

Keywords

Indirect Noise, Entropy Spots, Pressure Transducers

Introduction

Acoustic perturbations arising from the heat release in combustion devices has become a topic of increasing concern due to stricter noise regulations. Further pressure from the introduction of lean premixed pre-vaporised combustors, which burn more unsteadily, has increased noise emissions and the potential for catastrophic instabilities. In the last decade, a large effort has been undertaken to incorporate the information of jet noise in the design of combustors to reduce noise and instabilities whilst maintaining emissions benefits.

Combustion noise has traditionally been classified into direct and indirect combustion noise. The first is caused by isentropic pressure waves that are produced by the unsteady heat release and propagate towards the turbine (Lord Rayleigh 1894). In the second mechanism, local regions of hot gas (hot spots or entropy spots) are produced and then advected toward the turbine with the mean flow. These entropy spots are not directly associated with any pressure fluctuations in the linear regime. However, as they convect through regions with mean flow gradients (such as through turbine blades or exhaust nozzles) acoustic waves are created, generating indirect combustion noise. These waves travel both upstream into the combustor as well as downstream through the turbine. The upstream-travelling acoustic waves may couple with the acoustics of the system, stabilising or destabilising the original flame oscillation (Polifke et al. 2001; Goh and Morgans 2012). Marble and Candel (1977) originally developed a one dimensional analytical model, deriving expressions for the magnitude of both direct and indirect noise in the low frequency domain, and more recent work (Polifke et al. 2001; Goh and Morgans 2012; Stow et al. 2002; Durán et al. 2013) has revisited the issue.

Zukoski and Auerbach (1976); Bohn (1976, 1977) reported some of the first experiments attempting to isolate indirect noise by generating entropy spots synthetically using the Joule effect (electrical heating). However, due to the small temperature increase ($1K$) and the poor resolution of the data acquisition system, direct and indirect noise could not be separated. This method of generating hot spots was applied more recently in the Entropy Wave Generator (EWG) rig developed at DLR Berlin, to study indirect combustion noise (Bake et al. 2007, 2008, 2009a,b). Acoustic waves resulting from the unsteady electrical heating of thin wires were measured downstream of a convergent-divergent nozzle both in the subsonic and supersonic regime. The DLR experiment generated interest in the community and prompted multiple theoretical and numerical endeavours to explain the experimental results. Durán et al. (2013) performed simulations of the DLR EWG suggesting that in the case of the subsonic nozzle, the signal obtained was mainly due to direct noise, while in the case of the supersonic nozzle the signal was attributed to indirect noise and acoustic reflections (Leyko et al. 2011). In both cases the acoustic boundary conditions applied had a large influence on the results. Due to the difficulties in explaining the results of

[1]University of Cambridge, Engineering Department, UK

Corresponding author:
Francesca De Domenico, University of Cambridge
Email: fd314@cam.ac.uk

the DLR EWG experiment and the differing interpretations in the following analytical and numerical modelling (Bake et al. 2009b; Mühlbauer et al. 2009; Howe 2010; Leyko et al. 2011; Durán et al. 2013), further experiments have been developed to investigate the phenomena more in depth. The Osney Thermo Fluid Laboratory at the University of Oxford has produced an Entropy Wave Generator Test Rig (Hake 2014) where hot spots are also generated via electrical heating. At Politecnico of Milan a new concept of Entropy Wave Generator has been developed, based on the alternating injection of hot and cold air upstream of a high pressure turbine (Gaetani et al. 2015). Recent experiments have been performed in the Hot Acoustic Test rig at the DLR to investigate the sound generation and propagation due to accelerated cold spots in a nozzle (Knobloch et al. 2015).

The aim of all these experiments is to generate and isolate entropy noise in a clean and traceable way, without the complications induced by flames or vorticity, so that appropriate models can be suitably validated. Until now, there have been no measurements of the upstream entropy noise generated by the acceleration of synthetic hot spots: the experimental data refers only to the transmitted acoustic waves (acquired downstream of the nozzle). Yet the impact of the backward propagating waves is clear, as they can adversely affect the flame leading to instabilities (Polifke et al. 2001; Goh and Morgans 2012; Hochgreb et al. 2013).

The present experiment aims to generate synthetic and traceable hot spots via the Joule effect and detect the acoustic waves upstream rather than downstream of the nozzle. The results are intended to be complementary to the other experiments using EWGs. Further, the experiments highlight an issue previously unreported in the literature regarding the inadvertent use of condenser microphones in the low frequency range typical of entropy spot experiments, which can significantly alter the reported results.

Theoretical background

The theoretical underpinnings of the generation of acoustic waves via entropy spots in a flow have been discussed in a number of papers (Chu and Kovasznay 1958; Marble and Candel 1977), and further developed by Goh and Morgans (2012) and Durán et al. (2013). Most theoretical studies consider the one dimensional case of hot spots convecting through a compact nozzle. A schematic layout of this scenario is represented in Figure 1, where acoustic (P_2^+ and P_1^-) and entropy waves (σ) are generated in an unsteady heat release zone. The heat release zone is considered compact, meaning that its length is much smaller than all the wavelengths considered here (i.e. low frequency waves). These waves manifest themselves as fluctuations of pressure p', velocity u' and density ρ' relative to the mean flow pressure, velocity and density ($\bar{p}$, $\bar{u}$, $\bar{\rho}$), and can be represented by their respective amplitudes in the downstream (+) and upstream (-) direction, where (1) and (2) denote the regions upstream and downstream of the heat release interface:

$$P_2^+ \equiv \frac{1}{2}\left(\frac{p'}{\gamma\bar{p}} + \frac{u'}{\bar{c}}\right) \tag{1}$$

$$P_1^- \equiv \frac{1}{2}\left(\frac{p'}{\gamma\bar{p}} - \frac{u'}{\bar{c}}\right) \tag{2}$$

$$\sigma \equiv \frac{p'}{\gamma\bar{p}} - \frac{\rho'}{\bar{\rho}} = \frac{s'}{c_p} \tag{3}$$

Assuming negligible mean heat release ($\bar{q}$) and no incoming waves ($P_2^- = P_1^+ = 0$), Durán et al. (2013) derive expressions for the amplitudes of the waves generated at the heat release zone:

$$P_2^+ = \frac{1}{2}\left(\frac{\bar{M}}{1+\bar{M}}\right)q' \tag{4}$$

$$P_1^- = \frac{1}{2}\left(\frac{\bar{M}}{1-\bar{M}}\right)q' \tag{5}$$

$$\sigma = q' \tag{6}$$

where $\bar{M}$ is the mean Mach number and q' is the non-dimensionalised value of the fluctuating heat release $\dot{Q}'$ ($q' = \dot{Q}'/\dot{m}C_p\bar{T}$). These acoustic waves are referred to as 'direct' noise, as they are a direct result of the unsteady heat release.

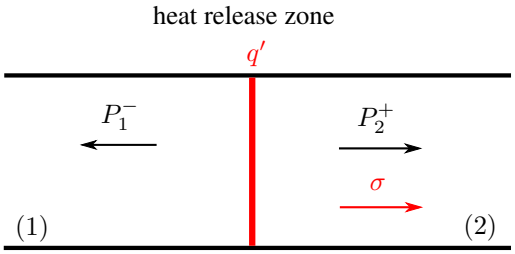

Figure 1. Waves generated at the heat release zone in the presence of a mean flow

The acoustic waves thus generated propagate at the speed of sound $\bar{c}$ relative to the mean flow, and are reflected at the inlet and outlet of the duct with reflection coefficients R_u and R_d, respectively (Figure 2).

The entropy spots are advected downstream with the mean flow without generating an acoustic signature in the linear approximation (Chu and Kovasznay 1958). If these waves are accelerated as they reach the duct outlet, they may generate acoustic waves which propagate both downstream and upstream of the outlet. In the case of a supercritical compact nozzle with an impinging isentropic hot spot, an expression for the amplitude of the backward (or 'reflected' wave) due its acceleration ($P_{2,s}^-$) is obtained as (Marble and Candel 1977):

$$P_{2,s}^- = -\frac{1}{2}\left(\frac{\bar{M}}{1+\frac{\gamma-1}{2}\bar{M}}\right)\sigma \tag{7}$$

The acoustic waves generated in this manner are referred to as 'indirect' noise, as they are only indirectly related to unsteady heat release upstream. Note that in this paper the terms 'indirect noise' and 'entropy noise' are used to indicate acoustic waves generated from the acceleration of entropy spots both upstream and downstream of the nozzle. Notably, this 'reflected' indirect noise is a negative perturbation relative to the mean, whereas the direct noise is positive.

In the absence of acoustic reflections at the boundaries, the shape of the direct and indirect acoustic waves in the time domain is expected to identical to that of the heat fluctuation q' (e.g. a square heat pulse should lead to a square acoustic pulse).

The experimental set-up described in this paper is designed to replicate the simplified one-dimensional case described above. Pressure and temperature are monitored using pressure transducers at selected locations. In general, such instruments are used in regions of their operation where their phase and gain are flat with frequency. Part of the purpose of the present experiment is to show how these gain characteristics are often neglected, leading to potentially erroneous outputs, so here we incorporate the instrument transfer function as part of the overall signal output.

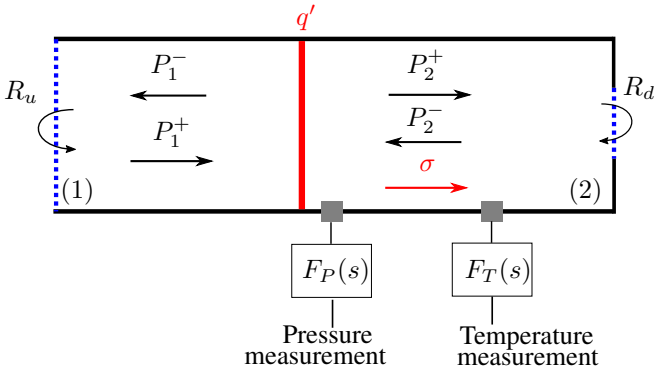

Figure 2. Experimental layout including pressure transfer function $F_P(s)$ and thermocouple transfer function $F_T(s)$.

Instrumentation

Experimental set-up

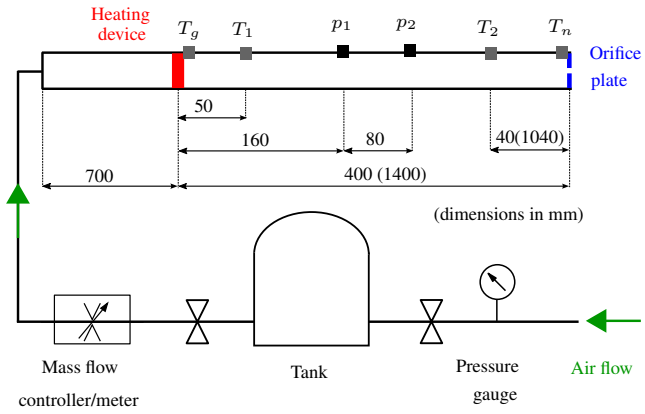

Figure 3. Schematic of the experimental set-up (values in parentheses correspond to the long tube configuration)

The experimental set-up is shown in Figure 3. Air flows through a tube at a controlled rate. Hot spots are generated synthetically by pulsing current through a heating device, generating a heat release pulse via the Joule effect. The air flow exits through an orifice plate, which can be operated in subsonic and sonic conditions. The hot spots are convected with the flow, and generate indirect noise as they accelerate through the orifice. Dynamic temperature and pressure measurements are performed downstream of the heating device, via flush-mounted pressure transducers or thermocouples, as described further on.

Filtered compressed air from the laboratory air supply system is fed into a 250 L tank to dampen out upstream pressure oscillations. The tank pressure is set to 5 bar using a pressure gauge. The tank is connected to the downstream tube via a 12 mm inner diameter plastic hose to a mass flow controller (MFC, Alicat MCR250, Acc. $\pm$ 1% FS), or a mass flow meter for high flow rates (MFM, Alicat MCR3000, Acc. $\pm$ 1% FS). The MFC/MFM are connected to the test section via a 12 mm, 1.2 meter long plastic hose via a flat flange to provide a simple boundary condition.

The tube has an inner diameter of 42.6 mm and is made from sections of PVC and stainless steel R16. The PVC tube inner diameter is slightly larger than the steel tube by 0.2%, so the discrepancy is assumed to be negligible. The different materials are used due to both safety and sealing considerations: the PVC pipe is lighter and easier to handle, but is prone to air leakages if fitted with transducer ports. Thus, it is used only in the sections of the tube where there are no transducers.

The heating device is fitted 700 mm downstream of the tube inlet via a PVC flange for electric isolation. The device itself is composed of three grids of thin tungsten wires (58 μm diameter) connected in series, with an overall resistance of about 1 Ω. Each module is made from 2.3 m of wire wound around a FR4 substrate, which keeps the wires in place using a toothed comb structure. Two copper plates connect the wires on both faces of the module, so that each heating grid is electrically equivalent to 42 parallel 45-mm-long resistances of tungsten wire. The heating device is roughly 10 mm thick, and therefore it can be approximated as a compact element for low frequency disturbances. An in-house circuit controlled by a computer drives a power supply, and delivers a current pulse of 21 A to the heating device, with a duration set to 200 ms for all the experiments.

The experimental set-up is flexible, and can be operated in several configurations to cover a large range of operating conditions. Two orifice plates are used: one with a 6.6 mm diameter hole (10 mm thickness), and a second with a 3 mm diameter hole (7 mm thickness). The length of the tube downstream of the heating device can be replaced to vary the convective length travelled by the hot spots. In the short tube configuration, the distance between the heating module and the orifice plate (convective length travelled by the hot spots) is 400 mm, whereas in the long tube case, this distance is 1400 mm.

The air temperature is determined with thin K-type thermocouples (fine gauge exposed welded tip thermocouples type K, 0.076 mm wire diameter, 1 m length, labelled T_i in Figure 3), whose time constant is found experimentally to be around 300 ms. In order to correct for the long response time relatively to the 200 ms heating pulses, a hot film anemometer (DANTEC gold plated wire probe type 55R01) with a wire diameter of 5 μm (response time under 10^{-4} ms) is used to obtain the shape of the temperature pulse. The pressure signal is acquired with condenser microphones and piezoresistive pressure transducers at the locations P_i: two G.R.A.S. 40bp (IEC 61094 WS3P 1/4") externally polarised condenser microphones connected to the G.R.A.S. 26AC 1/4" standard

preamplifier, two Kulite XTE-190(M) piezoresistive pressure transducers and a Kulite XT-140M piezoresistive absolute pressure transducer. The transducers are either placed on the same axial plane for calibration cross checking, or along the tube at stations downstream of the heating module. The outputs of the piezoresistive pressure transducers are amplified with a Fylde FE-379-TA modular DC amplifier. Both the Kulite and G.R.A.S. transducers are connected to a NI PCI-5259 board via a NI-2090 DAQ box. The sampling rate is 8192 samples per second, with a resolution of 16 bit.

Flow rate measurements and conditions at the throat

The flow meter/controller records the volumetric flow rate (Q), mass flow rate ($\dot{m}$), temperature T_f and pressure at the flowmeter P_f at a sampling rate of 20-30 Hz. The bulk flow velocity $\bar{U}$ is calculated as:

$$\bar{U} = \frac{Q}{A} \tag{8}$$

where A is the inner cross-sectional area of the tube. In the present analysis, the mean temperature in the tube $\bar{T}$ is assumed to be identical to that acquired at the flow meter T_f. The difference between these two temperatures is expected to be lower that 1%.

The Mach number at the orifice plate throat is necessary to estimate the intensity of the entropy noise, yet it is difficult to measure directly in subsonic conditions. An estimate for the Mach number M_T at the throat can be obtained by assuming isentropic expansion from the measured mean pressure in the straight section of the tube, $\bar{P}$, to the pressure at the throat, assumed to be atmospheric pressure ($P_T = P_a$).

$$M_T^2 = \frac{2}{\gamma - 1}\left[\left(\frac{\bar{P}}{P_a}\right)^{\frac{\gamma-1}{\gamma}}\left(1 + \frac{\gamma-1}{2}\bar{M}^2\right) - 1\right] \tag{9}$$

The upstream pressure $\bar{P}$ is measured with the Kulite absolute pressure transducer, and the upstream Mach number $\bar{M}$ is calculated from the bulk velocity and mean temperature ($\bar{M} = \bar{U}/\sqrt{\gamma R\bar{T}}$). Pressure losses across the orifice plate would produce lower real pressure ratios relative to the current estimate, yet the actual pressure at the throat is most likely lower than atmospheric until equilibration, so these two approximations act in opposite directions.

From the knowledge of the mass flow rate $\dot{m}$ and the calculated throat Mach number M_T, one can determine the effective area of the orifice, and therefore the vena contracta factor Γ, defined as the ratio of the actual mass flow rate to the one calculated using isentropic assumptions and the geometric area. From the conservation of the mass flow rate at the orifice location, as in Durrieu et al. (2001),

$$\dot{m} = \Gamma \rho_T A_T M_T c_T \tag{10}$$

The vena contracta factor Γ can be estimated as

$$\Gamma = \frac{A_1}{A_T}\frac{\bar{M}}{M_T}\left(\frac{1 + \frac{\gamma-1}{2}M_T^2}{1 + \frac{\gamma-1}{2}\bar{M}^2}\right)^{\frac{\gamma+1}{2(\gamma-1)}}. \tag{11}$$

where T indicates that the quantities are evaluated at the orifice location and 1 that they are evaluated in the straight section of the duct. From the literature, the vena contracta factor for a thick edged orifice is expected to be $\Gamma \sim 0.82$. The average vena contracta factor obtained with this method is 0.85 for the 3.0 mm orifice and 0.83 for the 6.6 mm orifice, which are close to the values described in the literature.

The dots in figure 4(a) show the upstream pressure $\bar{P}$ and velocity $\bar{U}$ measured in the tube at several operating points for the 3 mm and 6.6 mm orifice. The lines represent the theoretical relation between upstream pressure and velocity assuming an ideal isentropic convergent nozzle with a vena contracta factor $\Gamma = 1$ from Eqs. 9 and 11. Figure 4(b) shows calculated nozzle Mach number (obtained from Eq. 9) versus the upstream bulk flow velocity, comparing the experimental results with the theoretical predictions for an ideal isentropic convergent nozzle. The discrepancy between the ideal and measured case are due to the vena contracta factor Γ of the orifice.

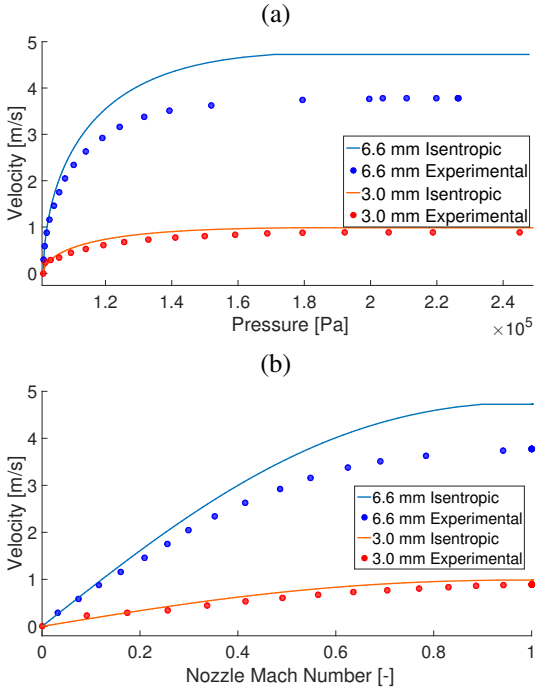

Figure 4. Calculated upstream duct bulk flow velocity *vs.* pressure (a), and calculated bulk velocity *vs.* calculated nozzle Mach number (b), for the 3.0 mm (red) and 6.6 mm (blue) diameter orifices. Lines represent the corresponding isentropic values $\Gamma = 1$.

Characteristics of the heating pulse

The experimental results are based on the assumption that two heating grids with the same characteristics behave identically under the same experimental conditions. The wires are prone to breakages given their small diameter, and the high current that is pulsed through them. A broken wire results in a short-circuit, and the heating module has to be extracted from the tube and rewound with 58 μm tungsten wires. Figure 5(a) shows the shape of the current pulse delivered to the heating module. The power supply delivers a maximum of 60 V and 21 A. In all the experiments the current is set to its maximum limit (I_{max}) while the

voltage is set to 35 V. This particular setting was found to be a good compromise to avoid frequent breakages while still inducing a significant temperature increase in the air flow. The heating module has a resistance $R \sim 1\ \Omega$, requiring a voltage $V = RI_{max} = 21$ V, and the excess energy is dissipated. However, in the first few milliseconds of the pulse, the capacitor in the driving system leads the power supply to release a higher current, before it auto-adjusts the current to its maximum nominal limit. The initial peak in the delivered current makes the wires warm up faster than they would do with a square pulse. Note that no filtering is applied to Figure 5(a) to avoid Gibbs fringes. It can be observed that there is no relevant time delay associated to the electric circuit: the time constant of the RC circuit is much shorter than the characteristic times of the experiment.

The time constant τ_w for the heating of a wire of diameter d_w, density ρ_w and specific heat capacity c_w cooled by an air flow with a speed of 1 m/s is calculated using a forced convection model for a heated cylinder in an air flow (Holman 2002):

$$\tau_w = \frac{\rho_w d_w c_w}{4h} \tag{12}$$

where h is the convective heat transfer coefficient. The expected time constant for a tungsten wire ($d_w = 58\mu$m, $\rho_w = 19300\ kg/m^3$ kg/m^3, $c_w = 130\ J/kgK$) and an air flow of 1 m/s ($h = 610$ W/m^2 K) is $\tau_w = 0.062\ s$. Therefore in the 200 ms duration of the pulse, the wires nearly reach their asymptotic temperature. Figure 5(b) shows the normalised and averaged (over 170 pulses) signal acquired with the anemometer 50 mm downstream of the heating module after the pulse (red solid line) and the analytical signal assuming a rising time of $\tau_w = 0.062\ s$ (blue line). In the heating process, the analytical pulse follows quite closely the shape of the experimental signal while, in the cooling process, the time constant is slightly higher. The power spectral density of the power signal obtained from the anemometer used to detect the temperature pulse is shown in Figure 6. Most of the energy of the signal is contained in the 0-100 Hz frequency range. Given that the experiments aim to acquire the forced response of the pressure to the low frequency heating pulse, the data are filtered with a 0-100 Hz ideal rectangular window digital filter.

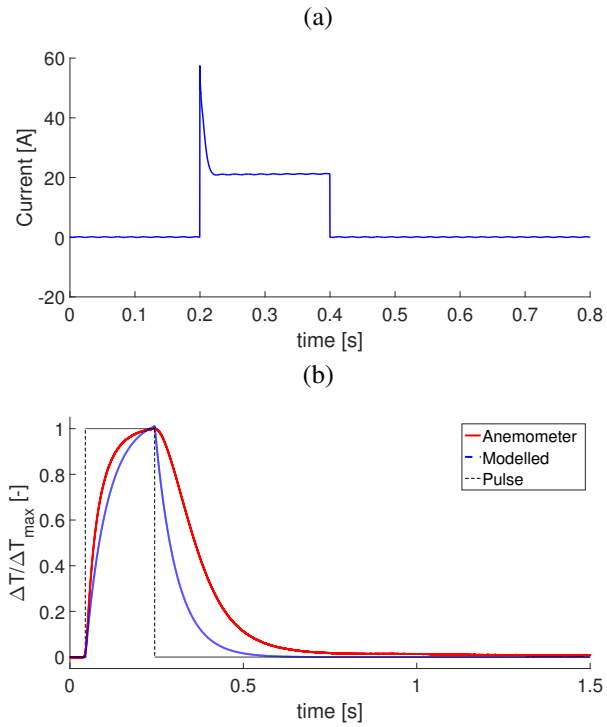

Figure 5. (a) Current pulse delivered by the driving system into the heating module; (b) normalised temperature rise profile of the hot spot signal acquired in the centre of the tube by the anemometer and analytical signal modelled with $\tau_w = 0.062\ s$.

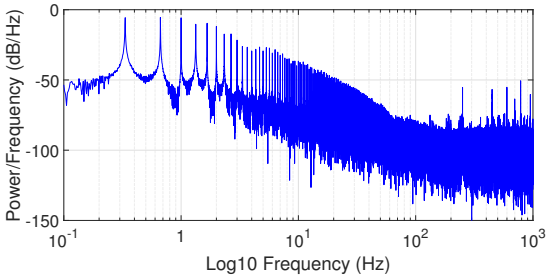

Figure 6. Power spectral density of the output of the forcing temperature pulse acquired with the anemometer 50 mm downstream of the heating module, for a mean flow velocity of 1f m/s.

Temperature measurements

Accurate information regarding the temperature and shape of the hot spots generated by the heating device is crucial to the understand and model the experiment. Three pieces of information are particularly important: the shape of the response of the temperature pulse in the time domain, the maximum temperature change induced in the air flow, and finally the spatial behaviour of the hot spots (how they spread and disperse before reaching the orifice). The transient nature of the heating process makes obtaining accurate measurements difficult. In order to overcome these difficulties, both thermocouple and hot wire anemometry measurements are performed simultaneously. Thermocouples are often used to determine a gas temperature, but for a given temperature input $T_I(s)$, they produce an output $T_O(s)$

$$T_O(s) = \frac{1}{1 + s\tau_{tc}} T_I(s) \tag{13}$$

where τ_{tc} is the time constant of the thermocouple. In order to reconstruct both the shape and the amplitude of the pulse precisely without applying further corrections, a transducer with a time constant at least one order of magnitude lower than the time constant of the heating module is required. Using the approach described in the previous section, this corresponds to a wire with a diameter smaller than 12.5 μm. However, the only commercial sensors of this size are bare wire thermocouples, which require shielding to withstand flows. It is difficult to manipulate such thin wires without breaking them and, once the wires are beaded, their time constant increases (Omega). In order to get around this issue, in this experiment, commercial beaded wire thermocouples with small diameters (0.076 mm) are used to obtain measurements of the asymptotic temperature rise.

For these thermocouples an average time response $\tau_{tc} = 0.3\ s$ was experimentally determined with a step input and an air flow of 20 m/s. For lower flow velocities, the time constant is higher. It is also observed that nominally identical transducers have a slightly different time responses owing to small differences during the manufacturing process, as shown in Figure 7.

The time constant and temperature rise of each thermocouple needs to be determined accurately to obtain sensible measurements of the hot spot temperature along the tube. To increase the accuracy, redundant measurements are carried out (several transducers in the same position and multiple acquisitions). The precision in the temperature rise was was obtained by pulsing the current through the wires for a sufficiently long time ($t > 3\tau_{tc}$) so the thermocouples reach their asymptotic temperature rise. The different measurements of the air temperature are kept as consistently as possible, but there is an estimated uncertainty of ± 2 K in the determination of the absolute value of the air temperature rise. This is due to: (i) difficulties in accessing the correct location for some measurements (*i.e.* as close as possible to the heating grid and to the nozzle), (ii) internal differences between the transducers, and (iii) small and uncontrollable variability of the test conditions (*e.g.* replacement of the heating module). The tests for acquiring the air temperature at the grid are performed with a open tube, to enable the thermocouple to be placed as close as possible to the heating grid. It is assumed that the same heating power delivered to the same mass flow rate leads to the same temperature increase in an open and closed tube configurations.

The hot wire anemometer is used to reconstruct the shape of the temperature pulse more precisely and determines the time constant of the wires and of the thermocouples. The 5 μm probe used has a negligible time response compared to the pulse duration, and, for moderate variations of the air temperature T_a ($\Delta T_a \sim$ 10-80 K), the functional dependence of the anemometer output voltage E can be expressed as a modified King's law (Bruun 1995):

$$E^2 = \frac{(R_1 + R_L + R_W)^2}{R_W}(T_W - T_a)(A + BU^n) \quad (14)$$

where R_L is the probe and cable resistance, R_W and T_W the hotwire resistance and temperature, U the bulk flow velocity, and A, B, n the calibration factor of the anemometer. It is assumed that after a heating pulse all the parameters in 14 remain constant apart from the output voltage $E_1 = E_0 + \Delta E$ and the air temperature $T_a = T_{a,0} + \Delta T_a$. For a given bulk flow velocity, the output voltages for the original and changed voltages are:

$$\begin{cases} E_0^2 = \alpha(T_W - T_{a,0}) \\ E_1^2 = \alpha\left[T_W - (T_{a,0} + \Delta T_a)\right] \end{cases} \quad (15)$$

where α is a proportionality constant.

$$\Delta T_a = \frac{E_0^2 - E_1^2}{\alpha} \quad (16)$$

From Eq. 15, considering that for a hot wire anemometer $T_W \sim 300\ ^\circ$C, and that in the present experimental conditions we have $T_W \gg T_{a,0} + \Delta T_a$, then Eq. 16 can be simplified as:

$$1 + \frac{\Delta E}{E_0} = \left(1 - \frac{\Delta T_a}{T_W - T_{a,0}}\right)^{\frac{1}{2}} \approx \left(1 - \frac{1}{2}\frac{\Delta T_a}{T_W - T_{a,0}}\right) \quad (17)$$

$$\Delta T_a = -2\frac{T_W - T_{a,0}}{E_0}\Delta E \approx -\beta \Delta E \quad (18)$$

Thus for small temperature increases, the change in the output voltage of the anemometer is in a first approximation proportional to the change in the air temperature and can be used to reconstruct the shape of temperature pulse.

Figure 7 shows how the actual temperature increase at a given location in the tube (in this case, just downstream of the heating grid) is reconstructed. First, the 200 ms long temperature pulse is acquired using a thermocouple. The thermocouple output is then corrected based on its time constant, and finally this result is compared with the temperature increase acquired after a 1.5 second long pulse to verify if the corrected temperature profile matches that of the long pulse output. Finally, assuming that the output of the anemometer captures the shape of the temperature pulse without distortion or attenuation, the shape of the temperature pulse is determined from the shape of the output voltage of the anemometer.

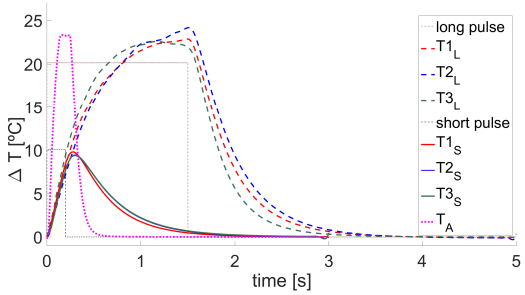

Figure 7. Temperature profiles acquired with three nominally identical thermocouples downstream of the heating grid, mean flow velocity of 1 m/s for a short (200 ms, Ti_S) and a long (1.5 s, Ti_L) pulse. Dashed lines: long pulse thermocouple measurements (color) and current pulse (black). Solid lines: short pulse thermocouple measurements (color) and current pulse (black). Anemometer output (T_A) normalised using the measured temperature rise.

Pressure transducer characteristics

Piezoresistive pressure transducers and microphones convert an acoustic signal into an electrical signal. Piezoresistive transducers rely on the piezoresistive effect which occurs when the electrical resistance of a material changes in response to applied mechanical strain (Carter et al.). They offer a flat frequency response and zero phase shift even at very low frequencies. Microphones translate pressure fluctuations into a voltage via a diaphragm or a cantilever beam exposed to the incident sound pressure, using cavities and vents as pressure equalisation channels. Microphones therefore act as as differential pressure measurements with capacitance, so that the sensors only respond to dynamic pressure fluctuations, unlike pressure transducers (Nielsen 1994; Zuckerwar 1995). The added capacitance means that their behaviour at low frequency drifts as a high pass filter,

with lower gain and shift in phase. On the other end, capacitive microphones are capable of higher sensitivity and dynamic range than piezoresistive pressure transducers.

The transfer function $F_p(f)$ of a condenser microphone such as the G.R.A.S. 40bp has been shown to be well represented by that of a high pass filter function (Carter et al.; Nielsen 1994):

$$F_p(f) = G\frac{i\frac{f}{f_0}}{1+i\frac{f}{f_0}} \tag{19}$$

where f_0 is the cut-on frequency of the microphone and G is the frequency-independent sensitivity of the microphone, called open-circuit voltage (Carter et al.). In the present work we calibrate the response of the condenser microphone to show that its corrected response can yield the original pressure data.

Predicted and measured transfer function of G.R.A.S. microphones The high pass filter behaviour of the two G.R.A.S. condenser microphones was measured at frequencies from 1 to 40 Hz, using a calibrated Kulite transducer as a reference, as these are not distorted at low frequencies. The experimental set up is shown in Figure 8: the test tube is attached by means of a conical intake to a plenum where two opposed loudspeakers are housed. The two loudspeakers excite the tube by generating sinusoidal acoustic waves of a given frequency. The loudspeakers are designed to operate above 48 Hz, but can be operated at lower frequencies, with additional harmonics superposed on the main signal, which can be easily filtered out. Here we use a lowest frequency of 1 Hz. All of the transducers are located on the same axial plane along the tube, exposing them to the same pressure signal in the plane wave approximation.

The differences in gain and phase between the signals acquired by the two G.R.A.S. microphones and the Kulite reference transducer are shown in Figure 9. As expected, the signals displayed by the G.R.A.S. transducers are attenuated (Fig. 9(a)) and phase shifted (Fig. 9(b)). The two G.R.A.S. transducers behave slightly differently at low frequencies. The cut-on frequency was experimentally determined as 1.02 Hz, with a phase shift of $\pi/4$. From the G.R.A.S. 26AC 1/4" standard preamplifier specifications, the cut on frequency of typical 1/4" microphones is around 1 Hz as expected. Indeed, from the specifications in the datasheet, the G.R.A.S. 40bp microphones have a frequency range ($\pm$2 dB) of 4 to 70 Hz.

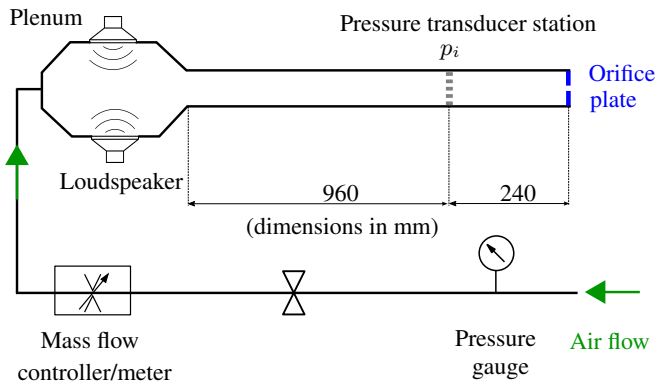

Figure 8. Schematic of the experimental set-up used to measure the low frequency transfer function of the G.R.A.S. microphones

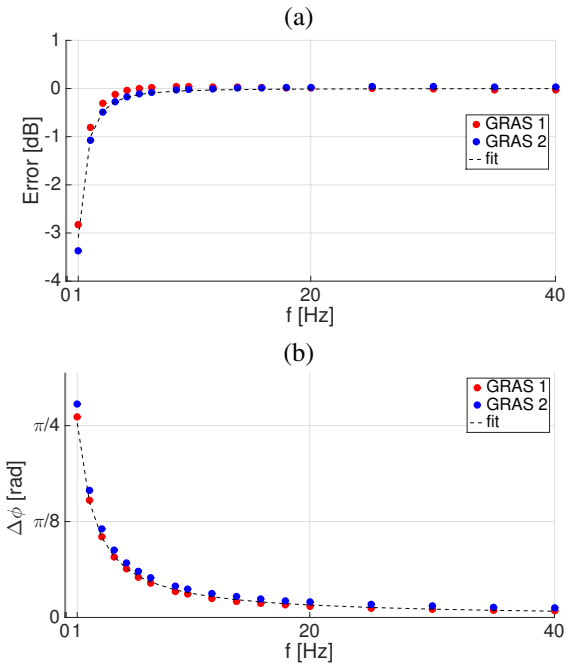

Figure 9. Difference in gain (a) and phase (b) between signals from the reference Kulite and G.R.A.S. transducers, along with a best fit curve (dashed) obtained from the experimental data.

Experimental demonstration of the signal distortion for capacitive microphones Prior to introducing tests with the heating device, low frequency pulsed excitation using a cold air pulse is used to test the G.R.A.S. sensor response relative to the Kulites, both with and without the corrected transfer function. Pulsating mass flow is injected by driving the mass flow controller with square pulses at 0.22 Hz frequency and a duty cycle of 15%. The mass flow controller valve rise time is only 7.4 ms according to the specifications. Measurements are carried out over a period of 32 seconds with a sampling frequency of 2048 Hz. Due to the presence of the orifice plate at the end of the tube, an increase in the flow rate leads to a pressure increase in the tube. Indeed, from Figure 10(a), it can be seen that the Kulite pressure transducers display the expected shape of the outputs in the form of a pressure rise to a final value, whereas the raw signal of the G.R.A.S. transducers produces a smaller rise and a ringing negative pulse at this low frequency.

The output from the G.R.A.S. sensors is corrected by the corresponding transfer function in Eq. 19 using the experimental values for f_0, as shown in Figure 10(b), producing an adequate match in their shapes and amplitudes.

Results

The response of the system to the generation and convection of synthetic hot spots was measured for four cases: (A) *open tube with flow*: open duct, with no orifice plate at the tube outlet; (B) *closed tube with no flow*, the tube is terminated with a rigid cap; (C) *accelerated flow (subsonic)*, the tube is terminated with the 6.6 mm orifice plate; (D) *accelerated flow (sonic)*, the tube is terminated with the 3.0 mm orifice plate, which is choked. These cases are summarised in table 1.

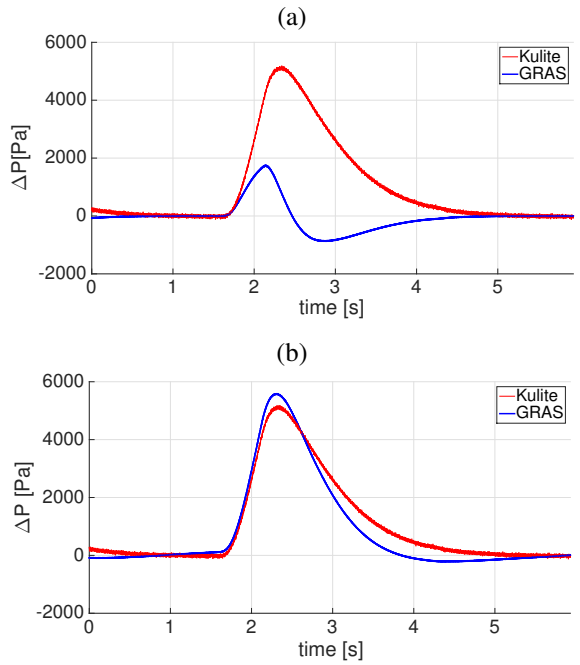

Figure 10. Pressure profile acquired after pulsating mass injection in the tube. G.R.A.S. microphone raw signal (a) and corrected by the transfer function (b).

The pressure signals shown in this section are acquired 160 mm downstream of the heating module. All the experiments are carried out in two configurations: a long tube configuration (400 mm convective length downstream of the heating module) and short tube configuration (1400 mm convective length).

A current of 21 A is pulsed for 200 ms with a voltage of 35 V; both the power and the energy are kept constant for all tests. The pulse period is set to 3 s to obtain a clear time separation between the acoustic oscillations caused by successive pulses. The air flow in the tube is varied between 75 and 205 slpm, which correspond to mean flow velocities of 0.88 m/s and 2.4 m/s, respectively. The acquisition time is set to 512 seconds, so that the signals are averaged over 170 pulses. The mean air flow temperature measured at the flowmeter varies between 19 and 21 K depending on the environmental conditions, and it is taken as 20 K on average.

Case	Description	Tube termination
A	Open tube with flow	Open tube
B	Closed tube without flow	Rigid wall
C	Accelerated flow (subsonic)	Orifice (6.6 mm)
D	Accelerated flow (sonic)	Orifice (3.0 mm)

Table 1. Overview of the four experimental cases

Case A: Open tube

Figures 11 and 12 show pressure signal results for Case A (open-ended tube) with a mean flow velocity $\bar{U}$= 2.16 m/s (upstream Mach number = 0.0063), in the short (a) and long (b) tube configurations, in the time and frequency domains. The acoustic pressure signal measured in the tube is very low, with a few peaks due to the gas expansion during heating. The theoretical reflection coefficient of an open end is close to -1, meaning that the forward propagating acoustic waves generated by the heating device (direct noise) are reflected at the outlet, and propagate back into the tube with an opposite sign. The pressure fluctuation signal is the sum of forward and backward waves in the tube, which explains why the pressure in the tube oscillates around zero. Given that the tube termination is an open end, the hot spots are not accelerated as they reach the outlet. There is therefore very little trace of direct noise, which is cancelled by the superposition of reflected waves with an opposite sign, and no indirect noise.

The fluctuations of pressure around zero are related to the acoustic time-scale (the time it takes for acoustic waves to propagate from the heating device to the tube boundaries). As such, in the short tube case, where the acoustic time-scale is short, the reflection occurs almost instantly, and the pressure in the tube is cancelled out almost immediately (Figure 11(a)). For the long tube, the acoustic time scale is longer, and the resulting fluctuations are larger, as the cancellation effect is delayed (Figure 11(b)). This response is analogous to a natural response of the system. From Figure 12, there is no pressure trace in the characteristic frequency band of the heating pulse (0-40 Hz). Instead, the period of the small oscillations that occur when the current is pulsed into the wires corresponds to the first natural frequency of the tube. Thus, the heating pulse excites the first natural mode of the pipe, but the oscillations are soon damped out. From the spectrum of the pressure signal (Fig. 12), the first natural frequency of the tube corresponds to a wavelength $\lambda \sim 4L$. The other peaks in the Fourier transform (Fig. 12) for both the short and the long tube configuration correspond to a open-closed tube configuration: calling f_n the frequency of the n^{th} peak, $f_n \sim c/(nL/4)$ where L is 1.1 m for the short tube and 2.1 m for the long tube. This suggests that the inlet of the 42.6 mm diameter tube behaves nearly as a closed boundary.

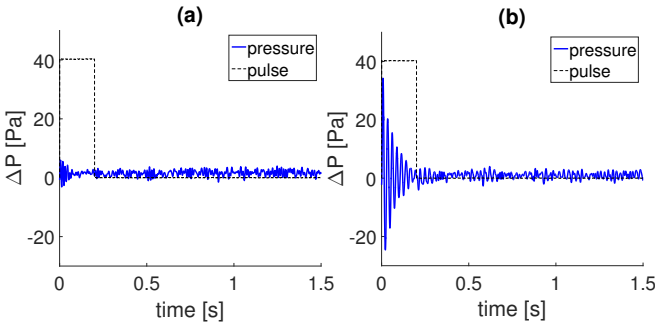

Figure 11. Ensemble-averaged pressure signals as a function of time obtained with an upstream Mach Number M=0.0063 and open tube in the short (a) and long (b) tube configuration.

Case B: Closed tube

Figure 13 shows the results for Case B (closed tube) with no mean flow. When the heating device is active, adjacent fluid is heated by conduction (the air trapped inside the tube is still) and tends to expand. The sudden expansion of the fluid, constrained by the inertia of the unperturbed media, creates a local pressure disturbance which leads to the generation of acoustic waves that propagate along the tube

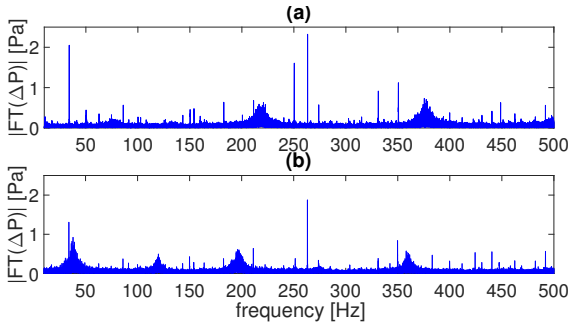

Figure 12. Ensemble-averaged pressure signal frequency signature obtained with an upstream Mach Number M=0.0063 and open tube in the short (a) and long (b) tube configuration.

at the speed of sound. The acoustic waves generated from the heat source impinge on the walls, and are reflected back. These waves repeatedly traverse between the boundaries, and are reflected back into the system, with the same sign as the original wave (the theoretical reflection coefficient at a rigid wall is 1). Given that the acoustic time-scale are an order of magnitude smaller than the pulse duration, these acoustic waves are essentially accumulating while the heating device is active. Once the heating device is switched off, these acoustic fluctuations decay due to losses at the boundaries, and viscous and thermal losses within the fluid (to a lesser extent) (Trilling 1955; Farouk et al. 2010).

Thus, in Case (B), the pressure signals shown in Figure 13 are the effect of direct noise generated while the heating device is active. These acoustic waves undergo repeated reflections at the two ends of the tube, which in this case behave similarly to two rigid walls. In a zero-loss situation, the reflection coefficients at both ends of the tube would be unity and the decay time of the acoustic signal would be infinite (no acoustic losses). However, the real part of the reflection coefficient at the inlet (mass flow controller) is slightly lower than unity, and the acoustic fluctuations inside the tube decay with a rate τ_D. For the short tube (blue line) the maximum pressure is higher and the pressure rises faster than for the long tube. Indeed, the tube boundaries are closer together, meaning that the acoustic time-scale is shorter, and the acoustic waves are reflected more times during a given interval than in the long tube configuration. As a result, the acoustic pressure build up in the tube is faster, leading to a higher maximum pressure.

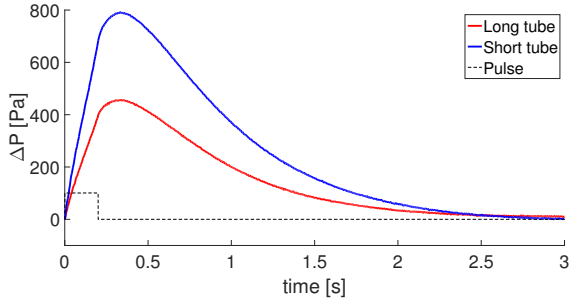

Figure 13. Ensemble-averaged pressure signals obtained after the heating pulse with closed boundaries (rigid wall at the end) for the short (blue line) and long (red line) tube configuration

Case C: Accelerated flow (subsonic)

In these experiments, the tube is terminated with the 6.6 mm orifice plate to accelerate the air flow. The experimental conditions tested are listed in table 2. From Figure 4 the bulk flow velocity required to choke the flow with the 6.6 mm orifice is 3.8 m/s therefore in test conditions listed, the flow through the orifice is subsonic.

	$\bar{P}$ $[kPa]$	$\bar{U}$ [m/s]	M_T	ΔT_g $[K]$	ΔT_S $[K]$	ΔT_L $[K]$
1	102.78	0.88	0.1429	26.7	19.1	7.9
2	103.54	1.11	0.1761	21.1	16.1	8.2
3	104.00	1.23	0.1933	19.5	15.1	8.0
4	105.19	1.46	0.2319	15.9	12.5	7.5
5	106.64	1.69	0.2713	13.3	10.9	6.8
6	108.34	1.91	0.3108	11.7	9.9	6.1
7	110.86	2.15	0.3608	10.5	8.5	5.9
8	113.65	2.40	0.4084	9.2	7.6	5.7

Table 2. Operating conditions for Case C (accelerated subsonic flow) for the long tube (1.4 m convective length downstream of the heating module) and the short tube (0.4 m convective length). $\bar{P}$: mean pressure at the grid; $\bar{U}$: bulk flow velocity at the grid; M_T: estimated Mach Number at the throat; ΔT_g: measured peak temperature rise of the hot spots at the grid; ΔT_S: measured peak temperature of the hot spots 0.4 m downstream of the heating module (location of the orifice plate for the short tube); ΔT_L: measured peak temperature of the hot spots 1.4 m downstream of the heating module (location of the orifice plate for the long tube)

Long tube Figure 14 shows the pressure signal obtained 160 mm downstream of the heating module in the long tube configuration. The velocity of the flow is kept low in order to obtain a clear time separation between the heating pulse and the time at which the hot spots arrive at the outlet. Since all the tests are performed by pulsing the heating device at a constant power, increasing the volumetric (and mass) air flow through the heating device decreases the measured temperature rise induced in the flow, as can be seen in Table 2. Two thermocouples are located in the orifice to detect the arrival of hot spots at the outlet of the tube. Figure 15(a) zooms on Case 3 to identify the characteristic components of the acoustic signal. The thermocouple output is not corrected: the application of the transfer function on the thermocouple signal has a non-physical anticipating effect on the signal.

Figure 15(b) reproduces the air temperature time history reconstructed from the output of the thermocouple and the anemometer using the method described previously. The data are recorded at three different convective lengths (L_c) downstream of the heating grid: 0.05 m, 0.4 m (end of the short tube) and 1.4 m (end of the long tube). The shape of the temperature signal close to the heating grid is has a higher peak, whilst for longer distances, the hot spot spreads out and the temperature signal is more disperse.

From Figure 15(a) a strong acoustic signal is observed in the tube while the heating device is active: there is a negligible time lag between the driving pulse and the the observed pressure pulse. For a distance $L_p = 0.16$ m between the heating grid and the pressure acquisition point, this time lag is of the order of $\tau_p = L_p/c \sim 5\ 10^{-4}$ s, which is of the order of the time resolution of the acquisition system ($\tau_S = 1/8192 \sim 1.2\ 10^{-4}$ s). Therefore, it can be concluded that this positive pressure oscillation represents

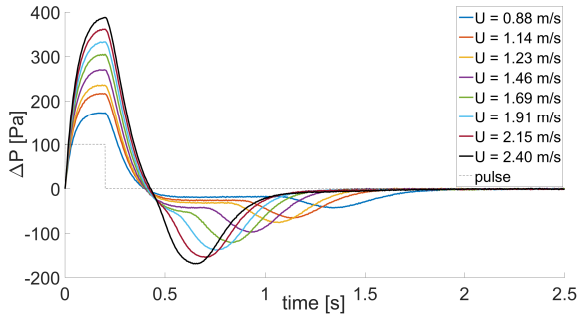

Figure 14. Ensemble-averaged pressure signal acquired by the Kulite transducer 160 mm downstream of the heating module for the cases listed in Table 2 (Long tube)

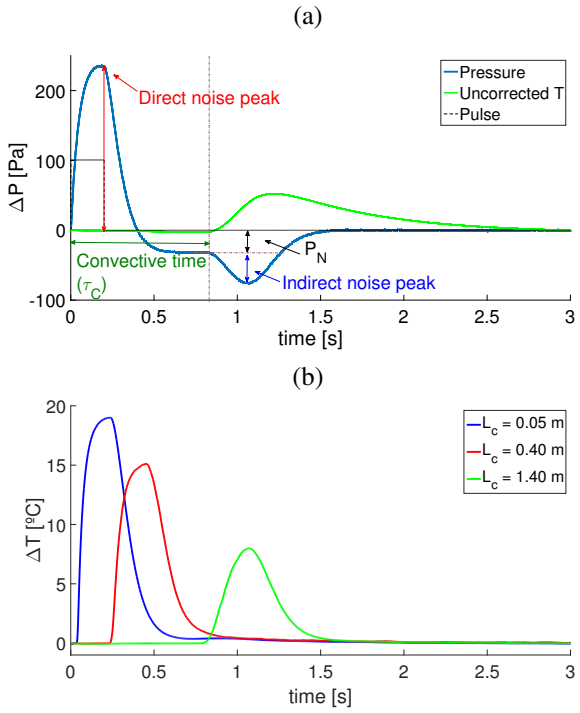

Figure 15. Detail of operating condition 3 (U = 1.23 m/s): (a) identification of direct noise, indirect noise, convective time; (b) reconstructed air temperature profile for three different convective lengths (L_C) downstream of the heating module (Long tube)

the direct noise. When the hot spot arrives at the orifice and is accelerated through it (which can be seen from the thermocouple signal), a smaller negative oscillation is observed. As the flow velocity increases (and the convective time decreases), this negative oscillation occurs earlier in time. Therefore, this negative peak is attributed to the acceleration of hot spots through the orifice plate, the so-called indirect noise. A third contribution to the acoustic signal can be seen in the pressure signal in Figure 15: after the direct noise peak, the pressure fluctuation does not return to zero, but becomes negative (negative oscillation labelled P_N). To explain this negative oscillation, Hwang and Kim (2006) suggests that, in the same way that air is expanded when the heating device is active, it is compressed when the grid is cooled, which causes this negative oscillation. Essentially, it is hypothesised that as the heating of the wires causes a positive pressure in the system, the cooling process creates a negative pulse in the system, and the negative oscillation P_N is the result of the small time delay between these the two processes. The fact that the amplitude of this negative oscillation increases as the mean flow is increased is consistent with this hypothesis.

Figure 16(a) shows the peak values of the direct and indirect noise against the estimated orifice Mach number. The indirect noise peak is evaluated by subtracting P_N from the minimum value of the pressure as shown in Figure 15(a). Both direct and indirect noise increase approximately linearly as the Mach number is increased, as expected from Eq. 4 and the limit for choked flow, Eq. 7. However, the amplitude of the direct noise is nearly four times larger than that of the indirect noise. Figure 16(a) shows that under subsonic conditions the effect of indirect noise is not negligible. Even at small Mach numbers at the orifice (i.e. low acceleration), and for small temperature fluctuations, there is still a clear sign of indirect noise, in contrast to to findings for subsonic conditions in previous experiments (Durán et al. 2013; Knobloch et al. 2015). In Figure 16(b), the maximum absolute values of direct noise and indirect noise from Figure 16(a) are normalised by the corresponding peak temperature increase of the air at the grid and at the nozzle from Table 1, and non-dimensionalised by the mean pressure and temperature in the tube. Both the normalised direct and indirect noise are directly proportional to the nozzle Mach number as expected. Considering that the peak temperature at the nozzle is on average half the value of the peak temperature at the heating grid, the normalised indirect noise becomes comparable to the normalised direct noise. However, for higher velocities, the ratio of the hot spot temperature at the nozzle and at the grid becomes smaller, which explains the different slopes of the two curves. This shows that in this experiment the direct noise has a significant influence and can not be neglected. The direct noise caused by the heating of the wires always reaches its maximum at the end of the heating pulse (t = 200 ms). As the flow rate (and the velocity) increases, the time separation between the direct noise and the indirect noise peaks becomes shorter, due to the decrease in the convective time. The convective time τ_C is determined as the point at which both thermocouples detect the arrival of the hot spot at the nozzle, and the Kulite pressure transducer detects the negative oscillation associated to entropy noise, as shown in Figure 15(a). The measured convective time using τ_C is listed in Table 3 for the eight cases in Figure 14. Those are compared to the mean convective time $\bar{\tau}$, calculated as the ratio between the distance L_C from the heating grid to the orifice plate and the bulk flow velocity ($\tau = L_C/\bar{U}$). The mean convective time is longer than the measured convective time by an average factor 1.38 ($\bar{\tau}/\tau_C = u_C/\bar{U} \sim 1.38$). As a result, using the bulk flow velocity to evaluate the time delay of the entropy noise would lead to an average error of 38%. This effect is attributed to the non-uniform velocity profile in the tube: the range of Reynolds number of the experiment is between 2400 and 6500 (transitional flow between a laminar and a turbulent jet), so that the flow velocity in the middle of the tube is substantially larger than the bulk velocity. Therefore, the velocity with which the hot air is convected in the central part of the tube is higher than the mean flow velocity.

These results suggest an important issue in the identification of indirect noise: increasing the flow velocity can

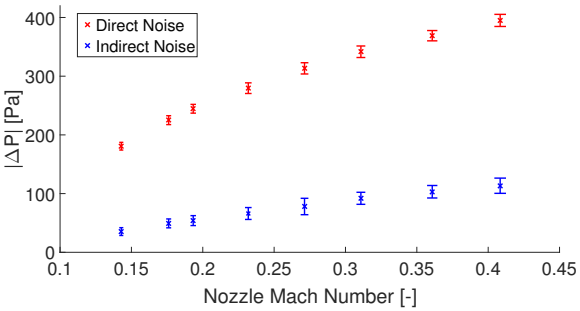

(a)

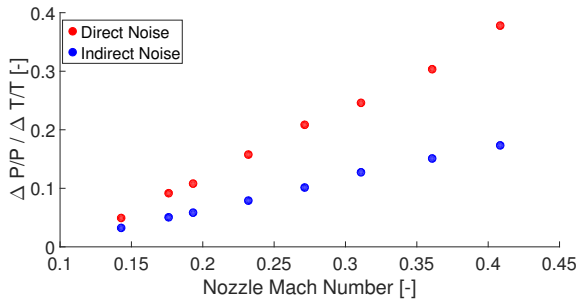

(b)

Figure 16. Absolute (a) and normalised (b) values of the peak of the acoustic oscillation of direct and indirect noise *vs.* estimated orifice Mach number in the long tube configuration

increase the relative contribution of indirect noise through acceleration in the nozzle, yet the convective time of hot spots decreases (Table 3). When the convective time becomes similar to the pulse length, direct and indirect noise start merging, and a clear time separation between the two is no longer possible. However, because the direct noise is typically higher (Figure 16), the effect of the indirect noise can not be individuated in a straightforward way: if this effect is not considered, it can be erroneously concluded that there is no indirect noise in the system.

	1	2	3	4	5	6	7	8
$\bar{\tau}$	1.59	1.25	1.14	0.96	0.83	0.73	0.65	0.58
τ_C	1.07	0.90	0.83	0.70	0.62	0.55	0.48	0.43
$u_c/\bar{U}$	1.49	1.40	1.38	1.37	1.34	1.33	1.36	1.35

Table 3. Comparison between the expected time delay of the indirect noise calculated using the bulk flow velocity ($\bar{\tau}$) and the convective time delay acquired experimentally (τ_C) (Long tube)

Comparison between the outputs of G.R.A.S. and Kulite transducers A note must be made regarding the usage of capacitive microphones in the present context. Figure 17 compares the pressure signal acquired by a G.R.A.S. microphone (green curve) and a Kulite pressure transducer (blue curve) for a bulk flow velocity of 1.26 m/s (M_1 = 0.0037) and a mean pressure in the tube of 103,500 Pa (case 3). The signal of the G.R.A.S. microphone is inverted to correct for the 180° polarity shift. The signal acquired by the G.R.A.S. transducer is both distorted and attenuated, and shows some non physical ringing caused by the high pass behaviour of the microphone. As expected, once this signal is corrected using the experimentally determined transfer function, it nearly matches both the shape and the amplitude of the signal obtained with Kulite transducer. However, while the match for the direct noise is relatively good, the negative pressure peak and the indirect noise peak are still slightly over predicted.

Why are the present findings regarding the different types of microphone relevant at all? In prior experiments aimed to generate hot spots and thermoacoustic waves with unsteady electrical heating of thin wires and foils (DLR EWG (Bake et al. 2009b), Oxford EWG (Hake 2014) and Hwang and Kim (2006), condenser microphones rather than pressure transducers were used. The same G.R.A.S. 40bp condenser microphones were used in the DLR EWG (Bake et al. 2009b), Panasonic electret condenser microphones (with a frequency range 20-20000 Hz) were used in the Oxford EWG (Hake 2014) and 40BP SV-CO were used in Hwang and Kim (2006). It is unknown whether the low-frequency response was taken into account in those cases, as this was not reported. However, two pieces of evidence suggest that they may not have been corrected: (i) in Bake et al. (2008), the figures shown (Figures 4, 5, 8) show the characteristic dip in pressure below zero, corresponding to the high pass filter behaviour of the capacitive microphones. Also in Figure 9 in Hwang and Kim (2006) the pressure signal displays ringings similar to the unphysical oscillations due to the high pass behaviour of the microphone that can be observed in Figures 10 and 17 ; (ii) in the simulation work by Bake et al. (2009b); Leyko et al. (2011); Durán et al. (2013), in order to reproduce the measured results mentioned in (i), the reflection coefficients for the anechoic end of the tube had to be manipulated and changed to what becomes a transfer function similar to the presently used high pass filter. The parameter $K = 160$ used in the simulations reported in Bake et al. (2009b); Leyko et al. (2011); Durán et al. (2013) corresponds to $f_0 = 12.73$ Hz, thus damps the 0 - 12 Hz acoustic components (Selle et al. 2004). Therefore, we suggest that in the future, all such low frequency measurements should be verified for accuracy according to the calibration measurements suggested here, or that piezo sensors be exclusively used for such measurements.

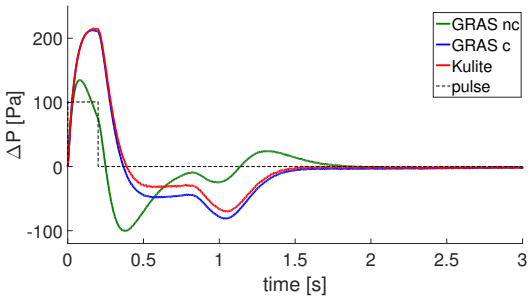

Figure 17. Ensemble-averaged pressure signal acquired 160 mm downstream of the heating module acquired by the Kulite pressure transducer (blue curve) and the G.R.A.S. microphone, before (green curve) and after (blue curve) correction using its high-pass filter behaviour at low frequencies (Case 3, long tube).

Short tube Figure 18 shows the pressure signal obtained 160 mm downstream of the heating module in the short tube configuration. From the results of Table 3, a convective time $\tau_C = 0.32s$ is estimated for the lowest flow velocity ($\bar{U}$=0.88 m/s), and $\tau_C = 0.12s$ for the highest flow velocity

($\bar{U}$=2.4 m/s). As a result of this much smaller difference in characteristic time, direct and indirect noise have merged, and it is no longer possible to analyse the two separately. This merging results in an apparent change both in the shape and the amplitude of the direct and indirect acoustic oscillations. The direct noise appears as a positive acoustic oscillation in the system, as observed in Figure 15, while the indirect noise brings a negative contribution: however, when they superpose, both the positive and the negative peaks decrease and the slope of the signal changes.

As shown in the case of the long tube, the amplitude of the direct noise is nearly four times higher than that of the indirect noise, and has a dominant effect on the pressure signal. This may lead to the indirect noise contribution to be underestimated or neglected altogether, and the direct noise contribution to be overestimated. This can be clearly observed in Case 8 ($\bar{U}$=2.4 m/s): the entropy spot reaches the nozzle 0.12 s after the beginning of the heating pulse, when the heating device is still active. The amplitude of the indirect noise peak seems smaller than in the $\bar{U}$=2.15 m/s case, whereas the direct noise is only slightly higher than in the $\bar{U}$=2.15 m/s case. However, as observed for the long tube configuration (Figures 14, 16) both direct and indirect noise contributions increase nearly linearly with Mach number. Thus, the apparent decrease in the indirect noise amplitude is an effect of the deconstructive interaction of direct and indirect noise. This interaction can also be seen in the shape of the the pressure oscillation: the sum of the negative oscillation with the positive direct noise peak effectively increases the decay rate of this positive oscillation.

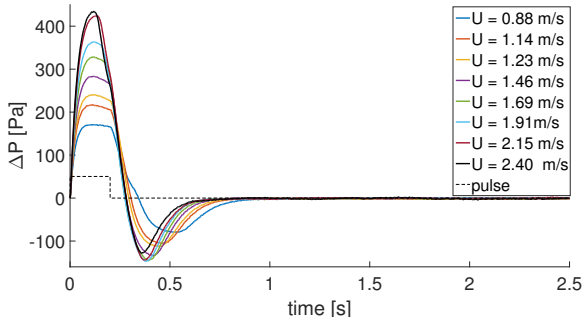

Figure 18. Ensemble-averaged pressure signal acquired by the Kulite transducer 160 mm downstream of the heating module for 8 bulk velocity cases between 0.88 m/s and 2.46 m/s (Short tube)

Case D: Accelerated flow (sonic)

Figures 18(a-b) show the pressure signals acquired in choked conditions with the 3 mm diameter orifice (red line) in the long and short tube configurations. From Figure 4 the pressure in the duct which corresponds to choked conditions is around 1.8 10^5 Pa. These results are compared with the corresponding results in the subsonic configuration (Case C, blue line), and with the closed tube case (Case B, purple line). The reflection coefficient of a choked nozzle is comparable to that of a closed end: the velocity is imposed at the throat, which thus nearly behaves as a rigid wall (apart from a small mean flow effect).

The shape of the pressure signal in the choked configuration can be understood by comparing it with the

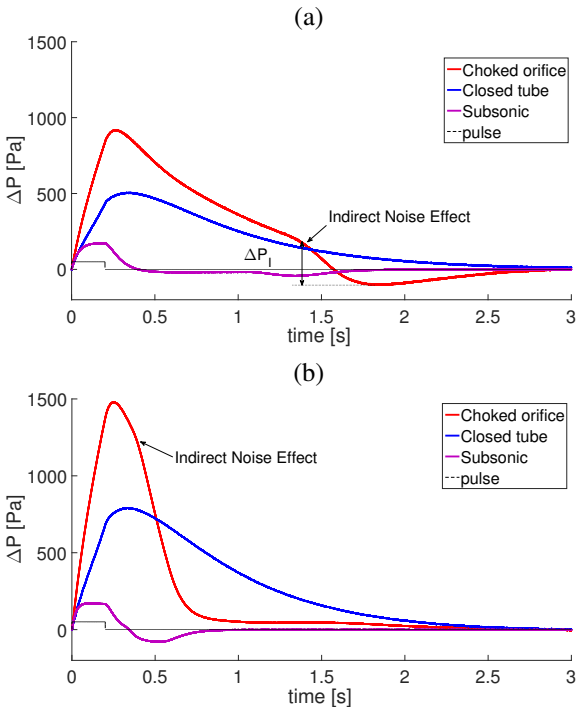

Figure 19. Averaged pressure signal acquired by the Kulite transducer 160 mm downstream of the heating module in the long (a) and short (b) tube. Red curves: choked tube; bulk flow velocity = 0.88 m/s (3 mm orifice); Blue curves: rigid wall (rigid wall with no flow); Purple curves: subsonic flow, bulk flow velocity = 0.88 m/s (6.6 mm orifice)

acoustic oscillations in the subsonic and in the closed tube case. Direct acoustic waves are created inside the tube when the heating device is active, and undergo repeated reflections at the two ends of the tube. Heat is exchanged from the heating device to the air via a convective mechanism, which is faster than the conductive mechanism in the closed tube condition, where the air is still. This results in a faster amplification of the acoustic energy in the system. When the heating device is no longer active, the acoustic energy starts to decay. The main difference relative to the closed tube appears due to the entropy waves: when the hot spots are accelerated through the nozzle, a negative acoustic oscillation is generated, which is manifested as a change of the slope of the pressure decay, which becomes steeper. However, the acoustic pressure only becomes negative in the case of the long tube configuration. Indeed, the indirect noise generation starts when the acoustic energy of the direct noise has yet to dissipate, and the sum of the positive oscillation resulting from the direct noise and the negative oscillation from the indirect results in the signal shape shown in Figures 19(a-b).

For the long tube configuration, the amplitude of the indirect noise can be estimated by isolating the negative pressure oscillation from the curve. The amplitude of this oscillation indicated is $\Delta P_I \sim 290$. Comparing this value with the indirect noise peak for the same bulk velocity in subsonic conditions, the indirect noise in choked conditions is nearly 10 times higher than in the subsonic conditions. With the short tube configuration, however, the amplitude of the indirect noise cannot be estimated in a straightforward way because the convection time of the entropy is too short

and the indirect noise signal can not be extracted from the overall acoustic signal, even if its influence as a change of the decay rate of the curve is clear.

Conclusions

In this paper we show measurements on an entropy generating rig with flexible configuration, driven by pulsed electrical heating, and aimed at measuring the resulting backward propagating acoustic signals from an orifice that is operated in subsonic and sonic conditions. The key result is the unambiguous identification of the contribution of direct and indirect noise in the overall noise. The acceleration of entropy spots is shown to generate a significant acoustic signal. To the authors' knowledge, a clear identification between direct and indirect noise for the reflected waves has not previously been demonstrated.

The indirect noise is isolated by choosing a convective time much longer than the electric pulse length. The indirect noise is then clearly identified by locating thermocouples in the orifice, which detect the arrival and acceleration of the hot spots: when the thermocouples start detecting an increase in air temperature, a negative pressure oscillation is detected by the pressure transducers. This negative pressure oscillation occurs earlier as the flow velocity is increased, due to a decrease in the convective time. We demonstrate that even for small flow accelerations (subsonic conditions), and small hot spot temperatures, indirect noise has a non-negligible contribution to the overall acoustic signal. However, direct noise is found to have a dominant effect: when the heating device is active, a large positive acoustic oscillation is detected by the pressure transducers. This pressure signal is caused by the air expanding due to the heat addition: no time lag is measurable between the heating pulse and this pressure pulse, which is therefore identified as direct noise. The peak amplitude of the direct noise peak is nearly four times higher than that of the indirect noise on average. From these results, it can be hypothesised that one of the reasons why the acoustic trace of entropy noise was not clearly detected in previous experiments is linked to the too short convective time of the hot spots. In this experiment, a clear time separation between direct and indirect noise can be obtained only at low flow velocities (1-2 m/s) and long convective distances (1.4 m). With higher bulk flow velocities and shorter convective distances, the contribution of the indirect noise merges into the higher direct noise and can no longer be easily identified, even if it may contribute.

Another key result is the need to carefully account for pressure transducer response at the very low frequencies typical of such rigs, which are limited by the cooling time of the wires. Condenser microphones behave as high pass filters, which significantly attenuate the pressure signal and lead to a phase shift at frequencies below about 10 Hz, and are unable to follow static pressure increases or decreases. This generates non-physical ringings in the displayed output, that can lead to a misinterpretation of the results.

Once the transfer functions of the microphones is taken into account, their outputs can be brought to a good agreement with piezoresistive transducers.

Outlook and further development

The comparison of the measurements and models requires the full characterisation of the tube acoustics at the relevant low frequencies, both regarding the reflection coefficient of the orifice plate as well as the upstream end. Whereas in general the orifice may be considered as a compact nozzle, potential losses need to be characterised for a fully quantitative comparison. Owing to the ultra-low frequency range of interest, the calculation of the reflection coefficients is not straightforward: even though the nozzle itself is acoustically compact, losses may need to be accounted for. Models for the transmissive and reflective properties of orifices can be found in the literature, but to the authors' knowledge, there is no information on their behaviour as a source of indirect noise. The theory for compact nozzles and diffusers (Marble and Candel 1977) underpredicts the entropy noise generated in this experiment, which suggests that it may possibly not be applicable to a plain orifice plate.

These experiments emphasise one of the major limitations of the current and previous set-ups: due to the physical behaviour of the wires, experiments can only be run in the ultra-low frequency range. This adds further complications to the understanding and modelling of the system due to the lack of experimental and analytical/numerical data in the infrasonic region. Moreover, the results are difficult to compare with a real physical situation. This suggests that it may be advantageous moving to configurations with a frequency range closer to the actual frequency range of the hot spot generation in real combustors, even if complications resulting from the hot spot generation methods arise.

Acknowledgements

Francesca De Domenico is supported by the Honorary Vice-Chancellor's Award and a Qualcomm / DTA Studentship (University of Cambridge). Erwan Rolland is supported by an EPSRC DTA studentship (University of Cambridge). Experiments were partly funded by EPSRC grant EP/K02924X/1. Francesca De Domenico gratefully acknowledges Dr. Davor Dukic for his help with the electrical part of the experiment, Luca Magri for valuable advice and G.R.A.S. staff for their technical support.

References

F. Bake, U. Michel, and I. Roehle. Investigation of Entropy Noise in Aero-Engine Combustors. *Journal of Engineering for Gas Turbines and Power*, 129(2):370, 2007. ISSN 07424795. doi: 10.1115/1.2364193.

F. Bake, N. Kings, and I. Roehle. Fundamental Mechanism of Entropy Noise in Aero-Engines: Experimental Investigation. *Journal of Engineering for Gas Turbines and Power*, 130(1): 011202, 2008. ISSN 07424795. doi: 10.1115/1.2749286.

F. Bake, N. Kings, a. Fischer, and I. Röhle. Experimental Investigation of the Entropy Noise Mechanism in Aero-Engines. *International Journal of Aeroacoustics*, 8(1): 125–141, 2009a. ISSN 1475-472X. doi: 10.1260/147547209786234966.

F. Bake, C. Richter, B. Mühlbauer, N. Kings, I. Röhle, F. Thiele, and B. Noll. The Entropy Wave Generator (EWG): A reference

case on entropy noise. *Journal of Sound and Vibration*, 326(3-5):574–598, 2009b. ISSN 0022460X. doi: 10.1016/j.jsv.2009.05.018.

M. S. Bohn. *Noise Produced by the Interaction of Acoustic Waves and Entropy Waves with High Speed Nozzle Flows*. PhD thesis, California Insitute of Technology, 1976.

M. S. Bohn. Response of a Subsonic Nozzle to Acoustic and Entropy Disturbances. *Journal of Sound and Vibration*, 52(2):283–297, 1977. ISSN 0022460X. doi: 10.1016/0022-460X(77)90647-2.

H. H. Bruun. *Hot Wire Anemometry: Principles and Signal Analysis*. Oxford University Press Inc., 1 edition, 1995.

S. Carter, A. Ned, J. Chivers, and A. Bemis. Selecting Piezoresistive vs . Piezoelectric Pressure Transducers. Kulite Semiconductor Products. AN 102. Technical report.

B. T. Chu and L. C. G Kovasznay. Non-linear Interactions in a Viscous Heat-Conducting Compressible Gas. *Journal of Fluid Mechanics*, 3:494–514, 1958.

I. Durán, S. Moreau, and T. Poinsot. Analytical and Numerical Study of Combustion Noise Through a Subsonic Nozzle. *AIAA Journal*, 51(1):42–52, 2013. ISSN 0001-1452. doi: 10.2514/1.J051528.

P. Durrieu, G. Hofmans, G. Ajello, R. Boot, Y. Aurégan, A. Hirschberg, and M C Peters. Quasisteady Aero-Acoustic Response of Orifices. *The Journal of the Acoustical Society of America*, 110(4):1859–1872, 2001. ISSN 00014966. doi: 10.1121/1.1398058.

B. Farouk, Y. Lin, and Z. Lei. Acoustic Wave Induced Flows and Heat Transfer in Gases and Supercritical Fluid. In Y. Cho and G. Greene, editors, *Advances in Heat Transfer (Vol.42)*, pages 1–136. Elsevier, 2010.

P. Gaetani, G. Persico, and A. Spinelli. Entropy Wave Generator for Indirect Combustion Noise in a High-Pressure Turbine. In *Proceedings of the 11th European Conference on Turbomachinery, Fluid Dynamics and Thermodynamics*, 2015.

C. S. Goh and A. S. Morgans. The Influence of Entropy Waves on the Thermoacoustic Stability of a Model Combustor. *Combustion Science and Technology*, (July 2015):120816123400009, 2012. ISSN 0010-2202. doi: 10.1080/00102202.2012.715828.

M. I. Hake. Experimental Design to Determine the Effect of Temperature and Mach Number on Entropy Noise. Technical report, Massachusetts Institute of Technology, 2014.

S. Hochgreb, D. Dennis, I. Ayranci, W. Bainbridge, and S. Cant. Forced and Self-Excited Instabilities from Lean Premixed, Liquid-Fuelled Aeroengine Injectors at High Pressures and Temperatures. In *Proceedings of the ASME Turbo Expo IGTI, June 3-7, 2013, San Antonio, Texas, USA*, pages GT2013—-95311, 2013. ISBN 978-0-7918-5511-9. doi: 10.1115/GT2013-95311.

J. P. Holman. *Heat Transfer*. McGraw-Hill, ninth edition, 2002.

M. S. Howe. Indirect Combustion Noise. *Journal of Fluid Mechanics*, 659:267–288, 2010. ISSN 0022-1120. doi: 10.1017/S0022112010002466.

I. J. Hwang and Y. J. Kim. Measurement of Thermo-Acoustic Waves Induced by Rapid Heating of Nickel Sheet in Open and Confined Spaces. *International Journal of Heat and Mass Transfer*, 49(3-4):575–581, 2006. ISSN 00179310. doi: 10.1016/j.ijheatmasstransfer.2005.08.025.

K. Knobloch, T. Werner, and F. Bake. Noise Generation in Hot Nozzle Flow. In *Proceedings of the ASME Turbo Expo 2015: Turbine Technical Conference and Exposition GT2015-43702*, pages 1–14, 2015.

M. Leyko, S. Moreau, F. Nicoud, and T. Poinsot. Numerical and analytical modelling of entropy noise in a supersonic nozzle with a shock. *Journal of Sound and Vibration*, 330(16):3944–3958, 2011. ISSN 0022460X. doi: 10.1016/j.jsv.2011.01.025.

J. W. S. Lord Rayleigh. *The Theory of Sound*. Macmillan, 1894.

F. E. Marble and S. M. Candel. Acoustic Disturbance from Gas Non-Uniformities Convected Through a Nozzle. *Journal of Sound and Vibration*, 55(2):225–243, 1977. ISSN 0022460X. doi: 10.1016/0022-460X(77)90596-X.

B. Mühlbauer, B. Noll, and M. Aigner. Numerical Investigation of the Fundamental Mechanism for Entropy Noise Generation in Aero-Engines. *Acta Acustica united with Acustica*, 95(3):470–478, 2009. ISSN 16101928. doi: 10.3813/AAA.918171.

T. Nielsen. Precision Microphone for Measurements and Sound Reproduction. In Michael Gayford, editor, *Microphone Engineering Handbook*, pages 62–139. Focal Press, 1994.

Omega. Website. URL www.omega.co.uk.

W. Polifke, C. O. Paschereit, and K. Doebbeling. Constructive and Destructive Interference of Acoustic and Entropy Waves in a Premixed Combustor with a Choked Exit. *Journal of Acoustics and Vibration*, 2001.

L. Selle, F. Nicoud, and T. Poinsot. The actual impedance of non-reflecting boundary conditions : implications for the computation of resonators. *AIAA Journal*, 42(5):1–21, 2004. ISSN 0001-1452. doi: 10.2514/1.1883.

S. R. Stow, A. P. Dowling, and T. P. Hynes. Reflection of Circumferential Modes in a Choked Nozzle. *Journal of Fluid Mechanics*, 467:1–25, 2002. ISSN 0022-1120. doi: 10.1017/S0022112002001428.

L. Trilling. Temperature Variations Induce a Sound Fields. *The Journal of the Acoustic Society of America*, 27(3):425–431, 1955.

A. J. Zuckerwar. Principles of Operation of Condenser Microphones. In G. S. K. Wong and T. F. W. Embleton, editors, *AIP handbook of condenser microphones*, chapter 2, pages 37–69. AIP press, 1995.

E. E. Zukoski and J. M. Auerbach. Experiments Concerning the Response of Supersonic Nozzles to Fluctuating Inlet Conditions. *Journal of Engineering of Power*, 98(1):60–64, 1976.